SANDIA REPORT
SAND2005-0840
Unlimited Release
Printed February 2005

Eye Safe Short Range Standoff Aerosol Cloud Finder

Thomas A. Reichardt, Ray P. Bambha, and Kevin L. Schroder

Prepared by
Sandia National Laboratories
Albuquerque, New Mexico 87185 and Livermore, California 94550

Sandia is a multiprogram laboratory operated by Sandia Corporation,
a Lockheed Martin Company, for the United States Department of Energy's
National Nuclear Security Administration under Contract DE-AC04-94-AL85000.

Sandia National Laboratories

Issued by Sandia National Laboratories, operated for the United States Department of Energy by Sandia Corporation.

Available to DOE and DOE contractors from
U.S. Department of Energy
Office of Scientific and Technical Information
P.O. Box 62
Oak Ridge, TN 37831

Telephone: (865) 576-8401
Facsimile: (865) 576-5728
E-Mail: reports@adonis.osti.gov
Online ordering: http://www.doe.gov/bridge

Available to the public from
U.S. Department of Commerce
National Technical Information Service
5285 Port Royal Rd
Springfield, VA 22161

Telephone: (800) 553-6847
Facsimile: (703) 605-6900
E-Mail: orders@ntis.fedworld.gov
Online order: http://www.ntis.gov/help/ordermethods.asp?loc=7-4-0#online

SAND2005-0840
Unlimited Release
Printed February 2005

Eye Safe Short Range Standoff Aerosol Cloud Finder

Thomas A. Reichardt and Ray P. Bambha
Remote Sensing and Energetic Materials
Sandia National Laboratories
P.O. Box 969
Livermore, California 94551-9056

Kevin L. Schroder
Exploratory Systems Technologies
Sandia National Laboratories
P.O. Box 969
Livermore, California 94551-9104

ABSTRACT

Because many solid objects, both stationary and mobile, will be present in an indoor environment, the design of an indoor aerosol cloud finding lidar (light detection and ranging) instrument presents a number of challenges. The cloud finder must be able to discriminate between these solid objects and aerosol clouds as small as 1-meter in depth in order to probe suspect clouds. While a near IR (~1.5-μm) laser is desirable for eye-safety, aerosol scattering cross sections are significantly lower in the near-IR than at visible or UV wavelengths. The receiver must deal with a large dynamic range since the backscatter from solid object will be orders of magnitude larger than for aerosol clouds. Fast electronics with significant noise contributions will be required to obtain the necessary temporal resolution.

We have developed a laboratory instrument to detect aerosol clouds in the presence of solid objects. In parallel, we have developed a lidar performance model for performing trade studies. Careful attention was paid to component details so that results obtained in this study could be applied towards the development of a practical instrument. The amplitude and temporal shape of the signal return are analyzed for discrimination of aerosol clouds in an indoor environment. We have assessed the feasibility and performance of candidate approaches for a fieldable instrument. With the near-IR PMT and a 1.5-μm laser source providing 20-μJ pulses, we estimate a bio-aerosol detection limit of 3000 particles/l.

CONTENTS

FIGURES

TABLES

1. Introduction

An eye-safe indoor aerosol cloud finding lidar (light detection and ranging) system presents a number of challenges. Many solid objects, both stationary and mobile, will be present in an indoor environment. The cloud finder must be able to discriminate between these solid objects and aerosol clouds as small as 1-meter in depth in order to probe suspect clouds with a UV fluorescence probe while minimizing personnel exposure to UV laser energy. A near IR (~1.6-μm) laser is desirable for eye-safety but the aerosol scattering cross section is significantly lower in the near-IR than at visible or UV wavelengths. The target aerosol particle density is expected to be between 10^5 and 10^6 particles/l. The receiver must deal with a large dynamic range since the backscatter from solid object will be orders of magnitude larger than for aerosol clouds. Fast electronics, (on the order of 1-ns rise times), with significant noise contributions, will be required to obtain the necessary temporal resolution. A glancing incidence on solid objects may produce a backscattered energy very similar to that from an aerosol. Finally, the production cost of a cloud finder must be low enough to consider putting it in a large number of facilities, constraining the choice of technologies and complexity of the system.

2. Approach

We have developed a laboratory instrument to look at aerosol clouds in the presence of solid objects. In parallel, we developed a lidar performance model for performing trade studies. Careful attention was paid to component details so that system performance could be accurately benchmarked. We have assessed the feasibility and performance of candidate approaches. The study concludes with the detection method that obtains the best sensitivity within the constraints of high probability of detection and low probability of false alarm.

The report is divided into eight remaining sections. The laboratory laser probe and detector are characterized in Sections 3 and 4, respectively, and these results are used to design an optical receiver in Section 5. Section 6 discusses calibration of the optical receiver. The system is used to detect controlled aerosol plumes, described in Section 7, and in Section 8 we extend these results to calculate detection limits for different detection schemes. Section 9 addresses the need of differentiating the aerosol plume from surface scattering, and the modeling approach and results are discussed in Section 10. Section 11 concludes the report with recommendations for future work.

3. Laser Probe

Laser Probe Description

The low-wavelength cutoff for eye-safe IR lasers is 1.4 microns. To use a laser source with output in the eye-safe range, initial studies were performed with a Sandia-built optical parametric generator (OPG) source, which produces 1.577 micron pulses, 2.2-nsec wide, at a 120 Hz repetition rate. However, the travel time through a 1-m plume is 3.3 nsec, and it was anticipated that the laser-pulse FWHM should be at least a factor of 2 less than this to differentiate the plume from surface scatter, which at normal incidence would generate a return signal equivalent to temporal profile of the outgoing pulse. Because the OPG produced pulses 2.2 nsec wide, it would not suitable for discriminating plumes ~1 m in depth from background surfaces. For demonstration purposes we therefore used the 1.064-μm output from a Litton Nd:YAG VEM 1064 series microchip laser. This source has a pulse length of 860 psec, a repetition rate >10 kHz, and a nominal pulse energy 4.7 μJ. While such a laser would likely not be appropriate for the final device, the results of detecting aerosol plumes with this Nd:YAG laser source can be scaled for a detection scheme with an eye-safe laser source.

Laser Probe Characterization

Previous aerosol backscatter studies with the OPG source demonstrated that our ability to detect a plume was limited by the acquisition of backscatter from multiple scattering events. We therefore recognized the need to match the laser divergence to the detector field-of-view (FOV), and undertook a careful design of the receiver/transmitter configuration. The Nd:YAG laser source was characterized by bringing the beam to a focus and measuring the beam radius with knife-edge measurements. A graph of the beam $1/e^2$ radius, or beam waist w, versus the distance from the lens z is shown in Fig. 1. The data are fit to a Gaussian beam modified by the M^2 parameter as follows:

$$w(z) = w_0 \sqrt{1 + \left(\frac{z - z_0}{z_R} \right)^2} \tag{1}$$

where

$$z_R = \frac{\pi w_0^2}{M^2 \lambda}. \tag{2}$$

In Eqs. (1) and (2), w_0 is the beam waist at the focus, λ is the laser wavelength, z_0 is the axial location of the focus, and z_R is the Rayleigh range (all in m). For a perfectly Gaussian beam, $M^2 = 1$; it is apparent from the fit parameters in Fig. 1 that the beam is very close to Gaussian.

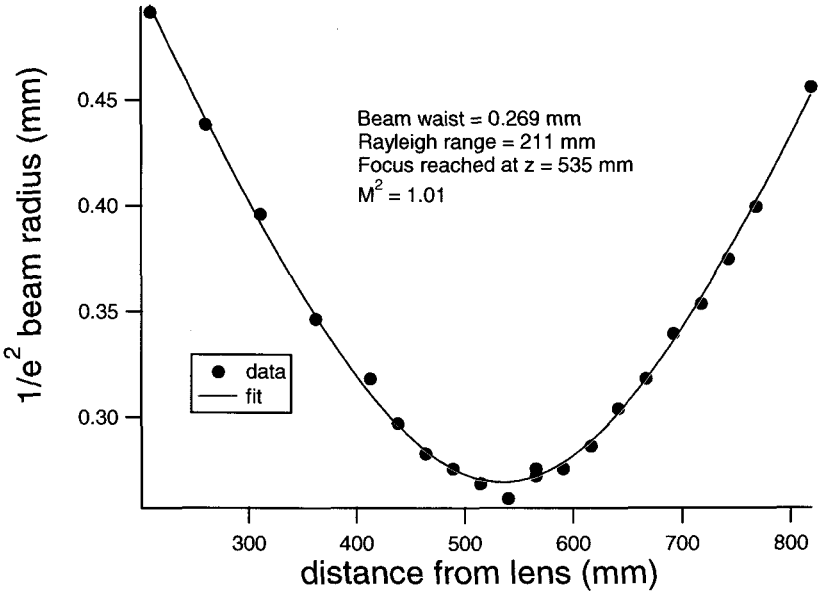

Figure 1. Spatial evaluation of laser probe. The beam was passed through an f = 91.2 mm lens placed 123 mm from the laser source.

Once the spatial characteristics of the laser beam were evaluated, and knowing the lens focal length and position with respect to the laser, we could determine the properties at the laser exit. The natural full-angle divergence from the source is calculated as 14 mrad, in agreement with the manufacturer's specifications. This divergence would allow a spatial resolution of 7-cm at a distance of 5 m from the instrument, which we judge appropriate for aerosol plume detection.

4. Detector

Detector Description

The detector is a Hamamatsu H9170-75 near-IR photomuliplier tube (PMT). This PMT is cooled to -60°C for operation and requires a vacuum pump to maintain this temperature. In addition to being the potential optimal detector, the PMT was judged as most versatile detector for evaluating the feasibility of implementing more compact, rugged detectors. The relevant characteristics of this PMT are listed in Table 1.

Table. 1. Specifications of Hamamatsu H9170-75 PMT.

Parameter	Value
Spectral response	950 to 1700 nm
Photocathode material	InP/InGaAs
Detection area for collimated light	19 mm
Area of PMT	2.0 mm
PMT operating temperature	-60°C
PMT supply voltage	-500 to -900 V
Quantum efficiency at 1064 nm	1%
Anode pulse rise time	0.9 nsec
Anode pulse fall time	1.7 nsec
Transit time spread	0.3 nsec
Diameter of condenser lens	20 mm
f/# of condenser lens	1.25

In addition to the specifications listed in Table 1, the PMT manufacturer measured and reported dynode gain values at three different bias voltages: gain = 2e+05 at -600 V, gain = 7e+05 at -700 V, and gain = 2e+06 at -800 V. Knowing that the gain is an exponential function of the bias voltage, we can write the relationship between the gain and bias voltage as follows:

$$\text{PMT gain} = 2 \times 10^{\left(\frac{|\text{bias voltage}|}{200} + 2 \right)} \tag{3}$$

which accurately describes the measured gain values, as shown in Fig. 2. The output of the PMT was measured with an Agilent Infiniium digital storage oscilloscope with an 8-GSa/s sampling rate and a 1.5-GHz analog bandwidth.

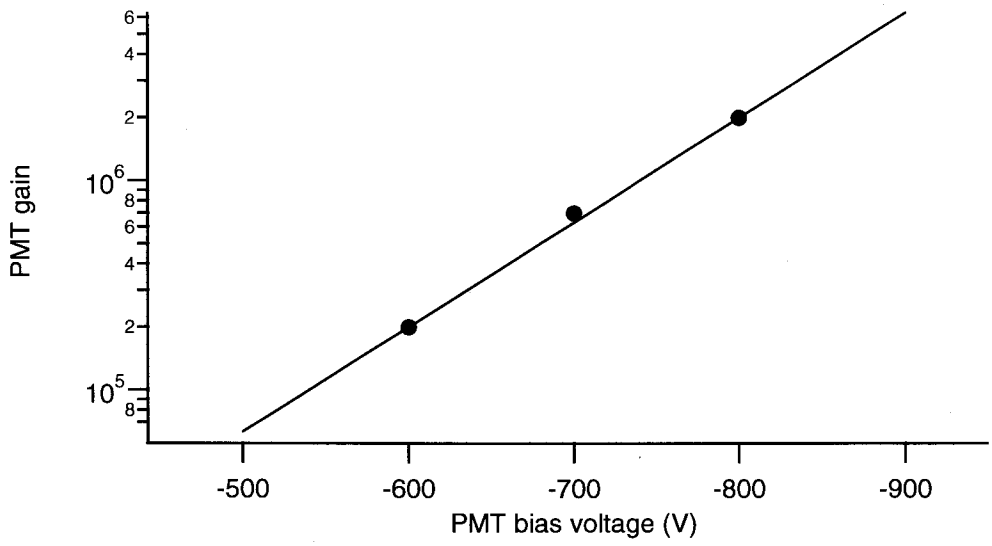

Figure 2. PMT gain as a function of bias voltage. The filled circles represent data from Hamamatsu, while the line represents an exponential function that accurately describes the data.

Detector Characterization

Unlike solid-state detectors, PMTs can often be saturated by only a few photoelectrons acquired over nanosecond time spans. For our demonstration instrument, it was desired to obtain backscattered signals on a single laser shot. Obviously, acquiring only a few photons from the target cloud would reduce the chance of detection. Reducing the bias voltage (and thus the gain) on a PMT can increase the number of photons that can be acquired before saturation, but this adjustment can also slow the detector response. We therefore undertook a systematic study of the PMT response to determine at which bias voltage we should operate in order to acquire the most photons before saturation significantly degraded the temporal response. The results of these studies are captured in Figs. 3-5. Figure 3 displays the FWHM of the output waveforms as a function of the peak-to-peak value of the waveforms. This figure demonstrates the effect of saturation on the width of the waveform: if the PMT detects too many photons, the waveform is temporally broadened. Note that as the PMT bias voltage is increased, the peak-to-peak signal at which saturation occurs is also increased. This relationship is displayed in Fig. 4, for which saturation was defined as the signal magnitude at which the waveform FWHM broadened to 2.2 nsec – 10% greater than its observed temporal response to single photons. Figure 5 shows another interpretation of the data displayed in Fig. 4, displaying the number of photoelectrons acquired at the onset of saturation as a function of PMT bias voltage. The peak-to-peak signal was converted to photoelectrons by the relationships

$$\#\,\text{electrons} = \frac{\text{signal[V]} \times \Delta t_{\text{pulse}}}{\text{resistance} \times \text{charge/electron}} = \frac{\text{signal [V]} \times 2\text{e-}9\,\text{s}}{50\,\Omega \times 1.6\text{e-}19\,\text{A}\cdot\text{s}}, \tag{4}$$

and

$$\#\,\text{photoelectrons} = \frac{\#\,\text{electrons}}{\text{PMT gain}}. \tag{5}$$

The number of photoelectrons required for saturation peaks at a PMT bias voltage of -550 V. For the remainder of results presented in this report, the PMT bias voltage was maintained at -550 V, while the laser energy is reduced so that the backscatter from the plume is was ≤24 mV.

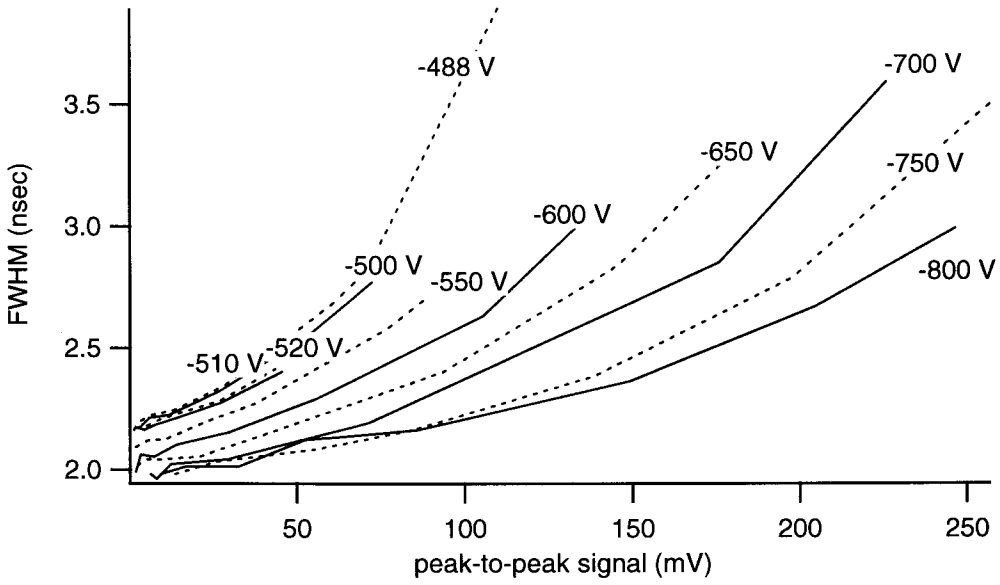

Figure 3. Signal FWHM versus signal magnitude.

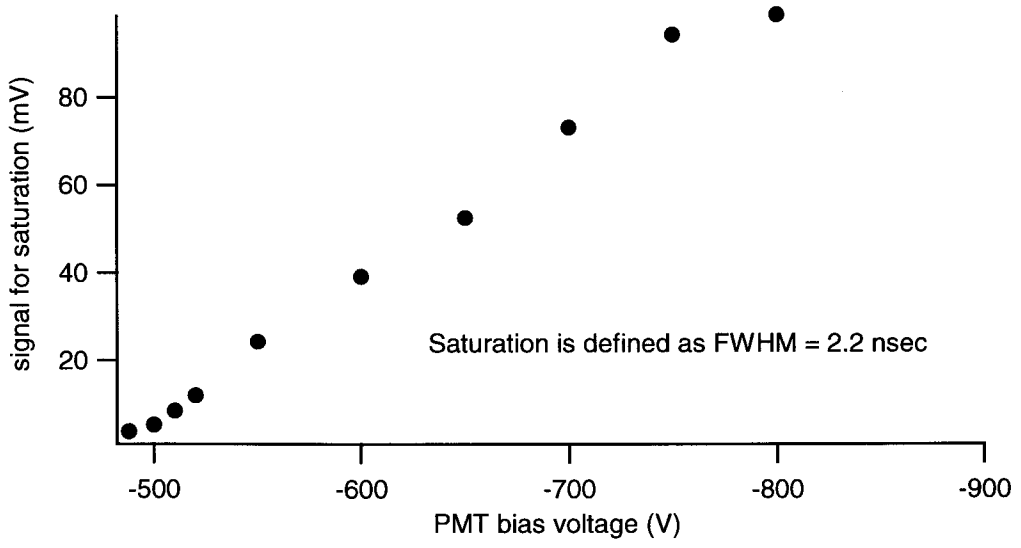

Figure 4. Signal level at onset of saturation as a function of PMT bias voltage.

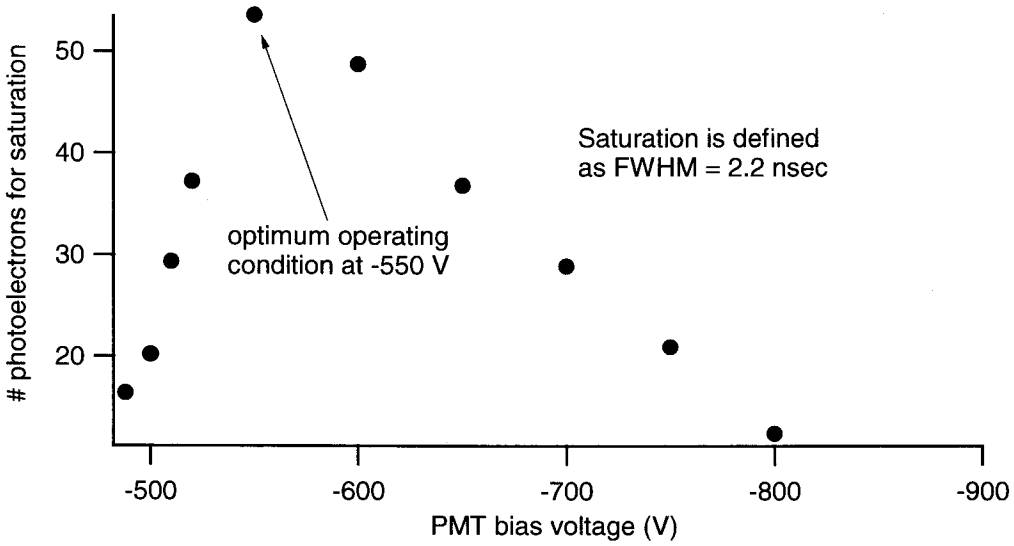

Figure 5. Photoelectrons acquired at the onset of saturation as a function of PMT bias voltage.

5. Optical Receiver Design

As listed in Table 1, the PMT possesses an f#/1.25 immersion lens with a 20-mm diameter. The focal length of this lens is therefore 25 mm, the far-field FOV of the PMT is 2 mm / 25 mm = 0.08 rad. This FOV is considerably larger than the divergence of the laser beam, and the receiver would therefore capture multiple scattering events and potential secondary reflections that would interfere with detection of the aerosol plume. We therefore designed an optimized receiver that matched the divergence of the laser beam.

Figure 6 displays the design of the optical receiver. It uses a two-lens system in conjunction with an aperture to form an external f-stop: lens A acts as the aperture stop, and the image of the probed area is focused between lens A and lens B. At this focus an aperture is placed to limit the angular divergence. Lens B then collimates the image for transmission to lens C, the fixed immersion lens with a 25-mm focal length.

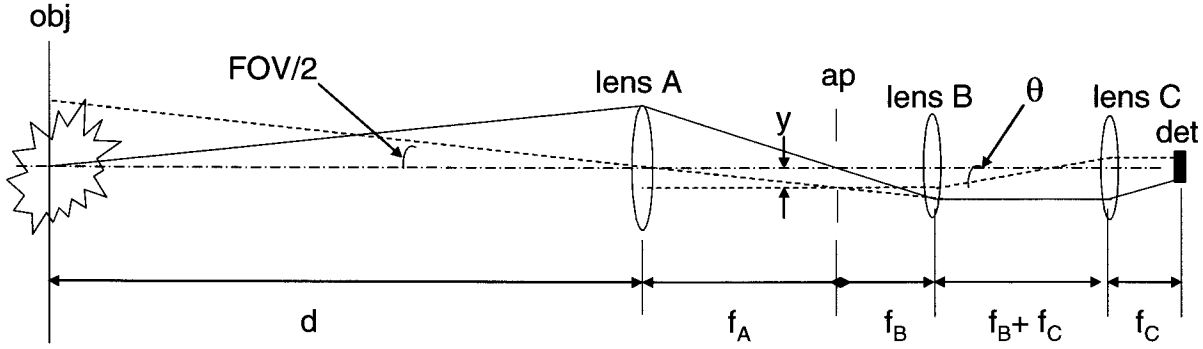

Figure 6. Optical receiver for limiting the FOV of the PMT. The solid line represents the collection aperture for the system, while the dashed line represents the FOV.

Lens A was selected to have a 500-mm focal length. For a FOV of 14 mrad, we see from Fig. 6 that the aperture diameter must be set to

$$\begin{aligned} \text{aperture diameter} &= 2 \cdot F_A \cdot \tan(\text{FOV}/2) \\ &= 2 \cdot 500\ \text{mm} \cdot \tan(0.014/2) \\ &= 7\ \text{mm}. \end{aligned} \tag{6}$$

We must also be careful to select the focal length of lens B so that the detector can collect the full FOV. From Fig. 6, for the detector to collect the FOV defined by the aperture,

$$\theta \le \tan^{-1}\left(\frac{\text{detector diameter}/2}{F_C}\right), \tag{7}$$

and θ(rad) is given by

$$\theta = \tan^{-1}\left(\frac{y}{F_B}\right) = \tan^{-1}\left[\frac{F_A \tan(\text{FOV}/2)}{F_B}\right], \tag{8}$$

so

$$\frac{F_A \cdot \tan(\text{FOV}/2)}{F_B} \le \frac{\text{detector diameter}/2}{F_C}. \tag{9}$$

Equation (9) sets the constraint $F_B \ge 88$ mm, and we chose $F_B = 129$ mm.

6. Transmitter/Receiver Calibration

After designing the receiver, it was necessary to check the system throughput to see if the returned backscatter signal agreed reasonably well with predictions. Laser pulses were directed to a Lambertian surface with a calibrated reflectivity of 0.12, placed 7.62 m away from the receiving lens (Lens A in Fig. 6). The laser energy was attenuated by over three orders of magnitude, transmitting only 2.0-nJ/pulse, to avoid saturating the PMT. The acquired backscatter signal was 19 mV. From standard LIDAR modeling, we expect that the ratio of received photons to transmitted photons would be

$$\frac{\text{received photons}_{\text{surface}}}{\text{transmitted photons}} = \frac{(0.12/\pi)A_{\text{lens}}T}{R^2}, \tag{10}$$

where A_{lens} is the area of the receiving lens (m^2), T is the transmission of the optical system, and R is the distance between the surface and lens A (m). The clear aperture of lens A is 42 mm in diameter, and the transmission of the spectral filter in front of the receiver is 0.57. In addition, the signal passes through three uncoated lenses, so each of the six surfaces is expected to transmit only 96% of the incoming light, reducing the overall receiver transmittance (including the spectral filter) to 45%. The expected ratio calculated from Eq. (10) is thus 4.1e-07.

Now we calculate the actual ratio of received photons to transmitted photons. Using Eqs. (3) - (5), and knowing that

$$\text{photons} = \frac{\text{photoelectrons}}{\text{quantum efficiency}}, \tag{11}$$

we calculate the number of received photons as 4200. The energy of an outgoing 1064-nm photon is hv, or 1.87e-19 J, and therefore the 2.0-nJ outgoing pulse contains 1.1e+10 photons. The ratio of received photons to transmitted photons is therefore 3.8e-07, in excellent agreement with the predicted ratio calculated above. Repeated tests with several transmitted laser energies yielded similar results.

7. Detection of Aerosol Clouds

To benchmark the system performance, we collected backscatter from aerosols generated by a Vicount 1300 smoke generator. The smoke generator outputs a well-characterized particle size distribution with the majority of particles ranging from 0.2 μm to 0.3 μm (see Fig. 7). This well-defined particle size distribution enables scaling the aerosol backscattering return signal studies to other aerosol sizes as well as other probe laser wavelengths. The smoke generator was operated with a supply pressure of 20 psi, producing only 20% of its rated maximum aerosol delivery rate (see Fig. 9), or 0.4 l/hr. The flow rate out of the 31-mm diameter nozzle was measured as 0.7 m/s, resulting in a volumetric flow rate of 0.53 l/s. If we assume an effective particle diameter of 250 nm, then the effective volume for a spherical aerosol particle would be 6.5e-20 m^3. The 0.4 l/hr aerosol delivery rate is therefore equivalent to a 1.7e+12 particles/s. Thus the particle density is given as

$$\text{particle density} = \frac{\text{particle flow rate}}{\text{total flow rate}} = \frac{1.7\text{e}+12 \text{ particles/s}}{0.53 \text{ l/s}} = 3.2\text{e}+12 \text{ particles/l} \qquad (12)$$

at the nozzle exit.

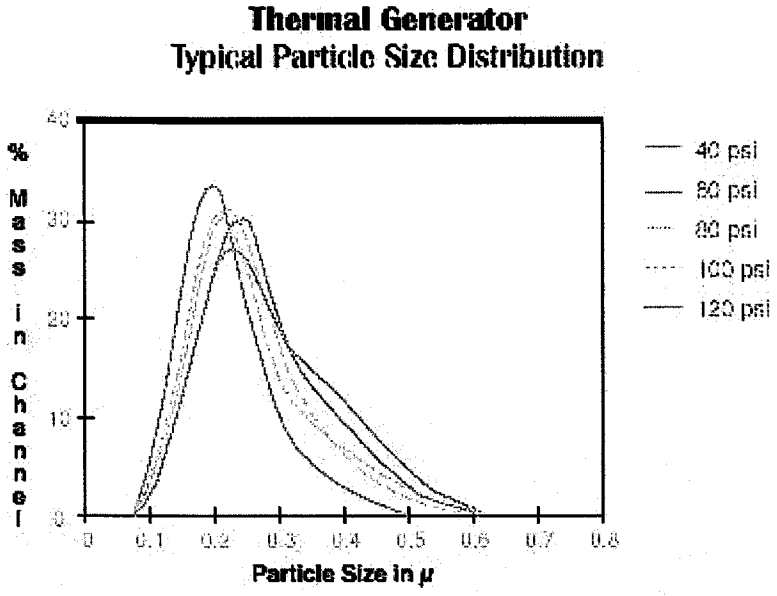

Figure 7. Particle size distribution for different supply pressures (acquired from manufacturer).

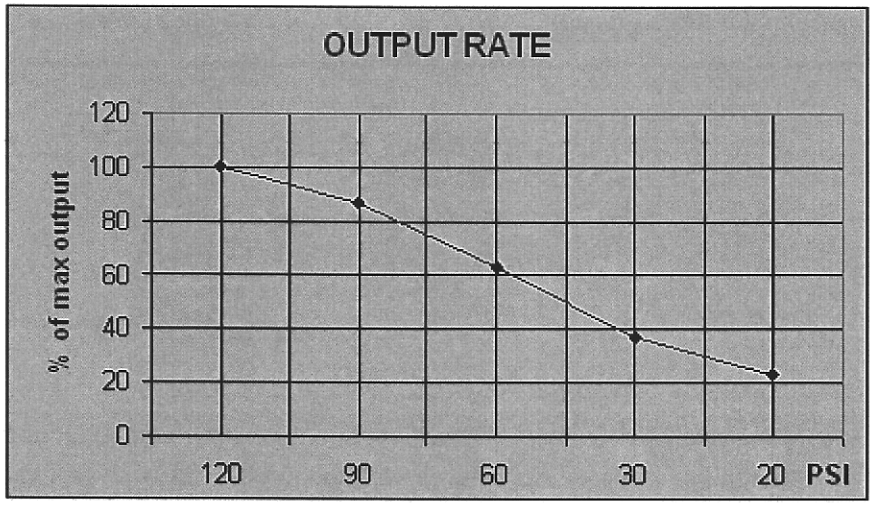

Figure 8. Smoke output rate as a function of supply pressure (acquired from manufacturer).

Figure 10 displays backscatter measurements with the aerosol plume placed at different distances in front of the calibrated reflectivity surface. The measurements were made at a location where the plume diameter had expanded to 23 cm. Analogous to Eq. (6) for surface backscatter, the expected return from aerosol backscatter is

$$\frac{\text{received photons}_{\text{aerosol}}}{\text{transmitted photons}} = \frac{\sigma\, N\, L\, A_{\text{lens}}\, T}{4\,\pi\, \mathrm{R}^2} \tag{13}$$

where σ is the scattering cross section (cm^2/sr), N is the particle concentration ($particles/m^3$), and L is the interaction length (m). Because the plume thickness is approximately the spatial length of the laser pulse, L can be approximated as the plume thickness. We have previously confirmed the hard-target backscatter agrees with predictions, and we can now approximate the scattering cross section of the particles by ratioing the signal return from the aerosol to that from the hard target. Observing the waveforms in Fig. 9, the signal return from the plume is 20% of the signal from the surface without the plume present. Ratioing Eqs. (13) and (10), we see that the relative signal return from an aerosol cloud, as compared to the return from the surface, is

$$\frac{\text{received photons}_{\text{aerosol}}}{\text{received photons}_{\text{surface}}} = \frac{\sigma\, N\, L}{4 \cdot 0.12} = \frac{\sigma\, N\, L}{4 \cdot 0.12} = 0.20 \tag{14}$$

Knowing that N is 3.2e+12 particles/l and setting L to the plume thickness, we calculate σ = 1.3e-10 cm^2. This is in reasonable agreement with the predicted cross section of 1e-10 cm^2 calculated for 300-nm spherical particles – the effective scattering cross section is weighted towards the larger particles – probed by 1064-nm light (assuming a refractive index n = 1.5).

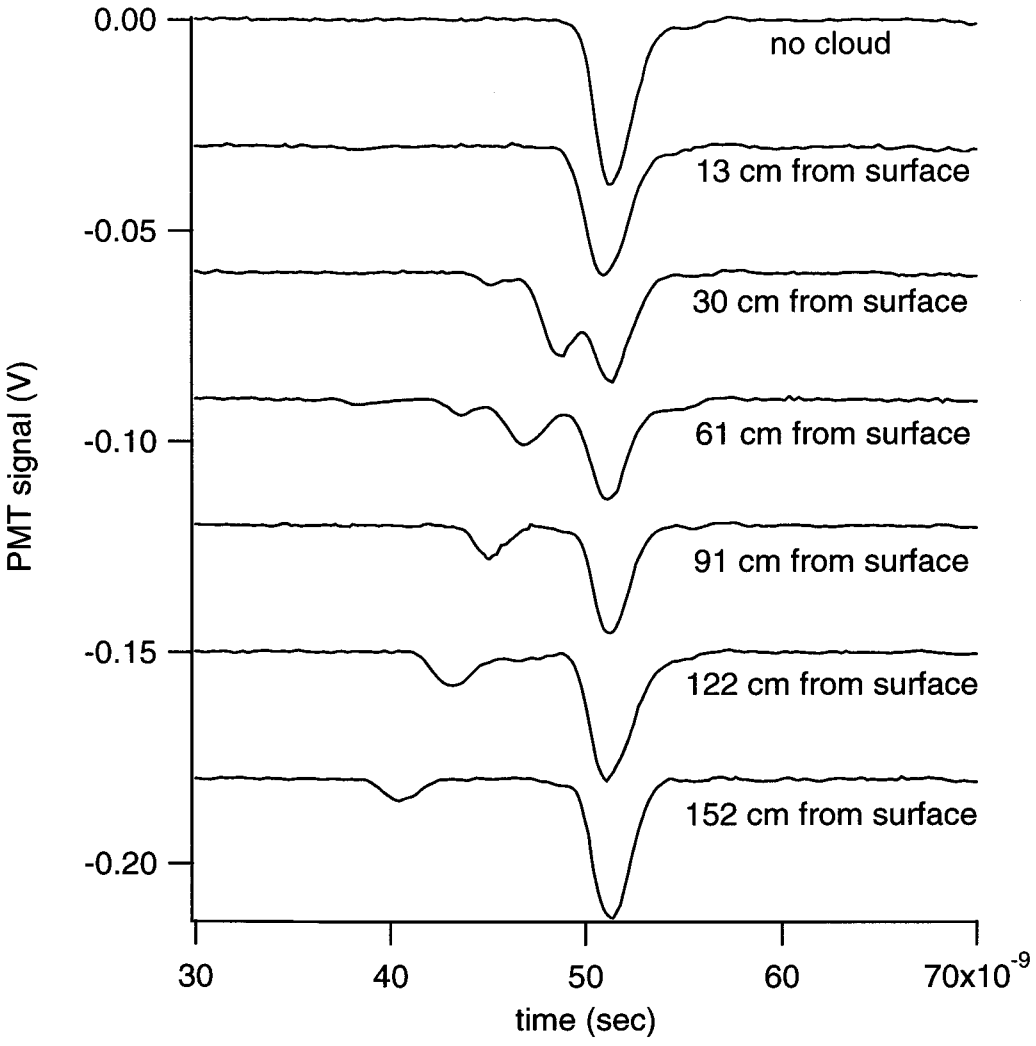

Figure 9. Aerosol backscatter for plumes at various distances in front of a surface with a 0.12 reflectivity. The laser pulse energy was 2 nJ.

8. Estimation of Detection Limits

Obviously, the smoke cloud described above has a particle density many orders of magnitude greater than is desired for an indoor biological aerosol detector. However, there are several factors that act in favor for extrapolating this approach for detection of biological aerosol plumes. For an eye-safe laser at 1.6 μm probing 3-μm particles, we expect the scattering cross section to increase by a factor of 100 as compared to probing the smoke particles with the 1064-nm laser.[1] From the PMT waveforms in Fig. 9, 8 mV of backscatter signal, or 18 photoelectrons, are being acquired for a plume with a particle density of 3.2e+12 particles/l. The backscatter signal from the solid surface is 38 mV, corresponding to only 4.0 nJ output energy. This laser energy can be increased by over three orders of magnitude: a fiber-laser pumped optical parametric generator could easily produce 20 μJ of 1.6-μm light for probing the scene. To calculate a detection limit, we will assume that 9 photoelectrons need to be acquired for plume detection, leading to a shot-noise-limited SNR of 3. Assuming that we would use a 2-in diameter collection lens as the receiving optic, we expect the following detection limit for biological aerosols probed with a single pulse of a 1.6-μm laser source:

$$\text{detection limit}_{\text{PMT}} = (3.2\text{e}+12\ \text{particles/l}) \cdot \frac{9\ \text{photons}}{18\ \text{photons}} \cdot \frac{4\text{e}-09\ \text{J}}{20\text{e}-06\ \text{J}} \cdot \frac{1\text{e}-10\ \text{cm}^2}{1\text{e}-8\ \text{cm}^2} \qquad (11)$$
$$= 3200\ \text{particles/l}.$$

While this detection limit is within the desired range, it would be much more practical to use a simpler, more compact near-IR detector (e.g., a solid state InGaAs photodiode) than to use the Hamamatsu PMT. The noise-equivalent power (NEP) for such a packaged detector (e.g., the New Focus 1611-FS-AC or the Newport AD series) is ~20 $\text{pW/Hz}^{1/2}$. Knowing that a bandwidth of ~1 GHz is required to temporally resolve the plume, the expected NEP for detection of the backscatter would be 6e-07 W. For a 1-nsec pulse, this noise is equivalent to 6e-16 J, or 5e+03 photons at 1.6 μm. To recognize a plume with a photodiode, we would likely have to collect three times this noise level, or 15e+03 photons. The single-pulse detection limit for biological aerosol plumes using a photodiode is therefore estimated as

$$\text{detection limit}_{\text{photodiode}} = (3.2\text{e}+12\ \text{particles/l}) \cdot \frac{15\text{e}+03\ \text{photons}}{1800\ \text{photons}} \cdot \frac{4\text{e}-09\ \text{J}}{20\text{e}-06\ \text{J}} \cdot \frac{1\text{e}-08\ \text{cm}^2}{1\text{e}-10\ \text{cm}^2} \qquad (12)$$
$$= 5\text{e}+07\ \text{particles/l}.$$

This is unfortunately well above the detection limit desired for indoor biological aerosol plumes. Therefore the Hamamatsu PMT or a similar device would be required to detect the presence of a biological aerosol plume.

---

[1] A. C. Eckbreth, Laser Diagnostics for Combustion Temperature and Species. 2nd ed. Gordon and Breach, Amsterdam, The Netherlands, p. 187.

9. Plume Recognition

Our final studies with the laboratory system focused on the true capability of the instrument to recognize aerosol plumes, differentiating the aerosols from surface targets. Because the temporally resolved signal is acquired at such a high bandwidth, we should be able to differentiate aerosol scatter from surface scatter by the rise time of the acquired waveform. This expected difference in rise time is even evident in the top two waveforms in Fig. 9 for the 23-cm thick plume. The backscatter rise time is 1.250 nsec for the solid surface (the PMT was somewhat saturated from the surface backscatter), and the presence of the plume located next to the surface increases the rise time to 1.375 nsec.

For the isolated plumes displayed in Fig. 9 the difference in rise time is less obvious. The plume thickness approximately matches the laser pulse width, and therefore backscatter from the plume shows similar temporal characteristics to surface backscatter. For reliable detection the plume should be considerably wider than the laser pulse, so experiments were performed at points where the plume had expanded further. Figure 10 displays the waveform resulting from probing a larger plume. The 10-90% rise time of the aerosol backscatter is 2.25 nsec, significantly longer than the corresponding rise time of the surface backscatter (1.12 nsec).

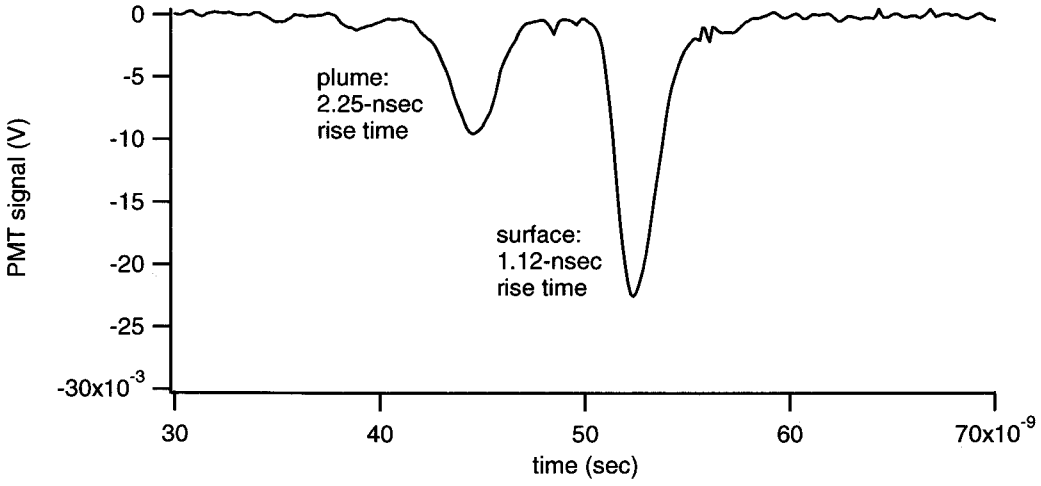

Figure 10. Plume identification by measuring rise time of backscattered signal.

A factor yet to be considered is that the laser beam will reflect and scatter off of solid objects at a variety of incidence angles. Unless the target is at normal incidence, it will appear to the lidar system to have an effective depth, a function of both the angle of incidence on the surface as well as the laser beam diameter. This depth will act to temporally broaden the return signal. The backscattered waveforms in Fig. 11 were all acquired from our Lambertian scatterer placed at different angles of incidence with respect to the laser beam path. The waveform temporally broadens as the angle of incidence increases. This temporal broadening could result in a glancing incidence return being mistaken for an aerosol cloud. However, we note that the backscatter return from a solid object, even at glancing incidence, will be much larger than the aerosol backscatter. Potentially the plume could be differentiated from glancing incidences by measuring both the temporal rise-time and the amplitude of the return signal. Detailed modeling should be performed to optimize the laser/detector format, covering the area in the appropriate time while minimizing the chance of a false positive.

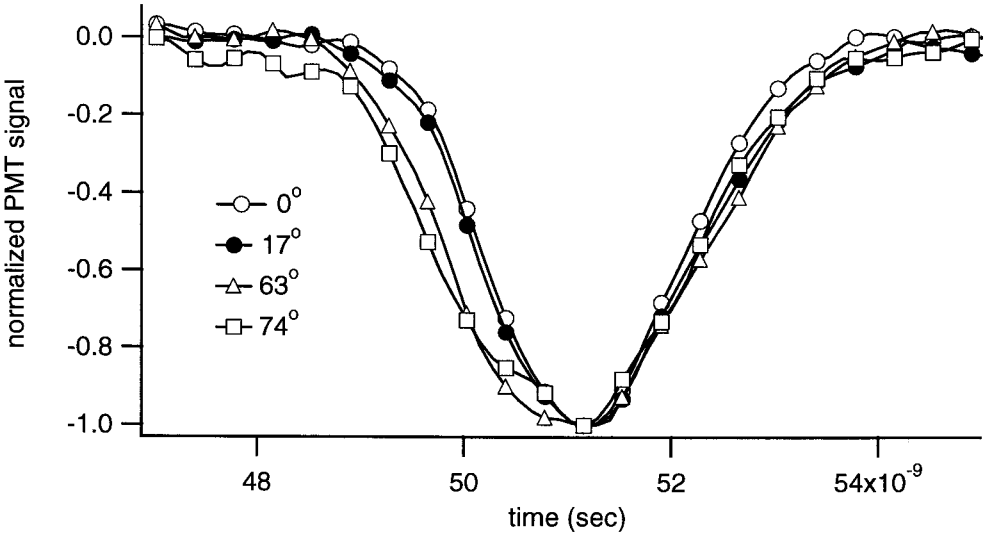

Figure 11. Backscattered signal for different solid glancing incidences. The waveforms have been normalized to unity and temporally shifted so that the peaks coincide.

10. Modeling of Plume Detection

In parallel with the experimental studies, we have developed a lidar performance model for performing trade studies. The model accounts for the range to the plume, the wall reflectivity, plume parameters (particle density, size, and index of refraction), receiver filter characteristics, detector noise, and A/D quantization errors. Including effects of finite pulse duration, range, and finite receiver filter bandwidth, the power received as a function of time is[2]

$$P(t) = P_o \int_0^{ct/2} dr \frac{A_0\, \sigma(r)\, \delta_x}{r^2} \int_0^{-2r/c} h\left(t - 2r/c - t'\right) e\left(t'\right) dt' \qquad (13)$$

where P_o is the average power in the pulse (W), A_o is the objective area (m^2), h is the receiver filter impulse response, $\sigma(r)$ is the plume backscatter profile, δ_x is the laser pulse width, and $e(t)$ is the laser temporal pulse shape. Sample results from this modeling effort are shown in Fig. 12. The plots on the left correspond to a detector with an NEP of 20 $pW/Hz^{1/2}$, while the plots on the right correspond to a lower detector noise level, NEP = 2 $pW/Hz^{1/2}$.

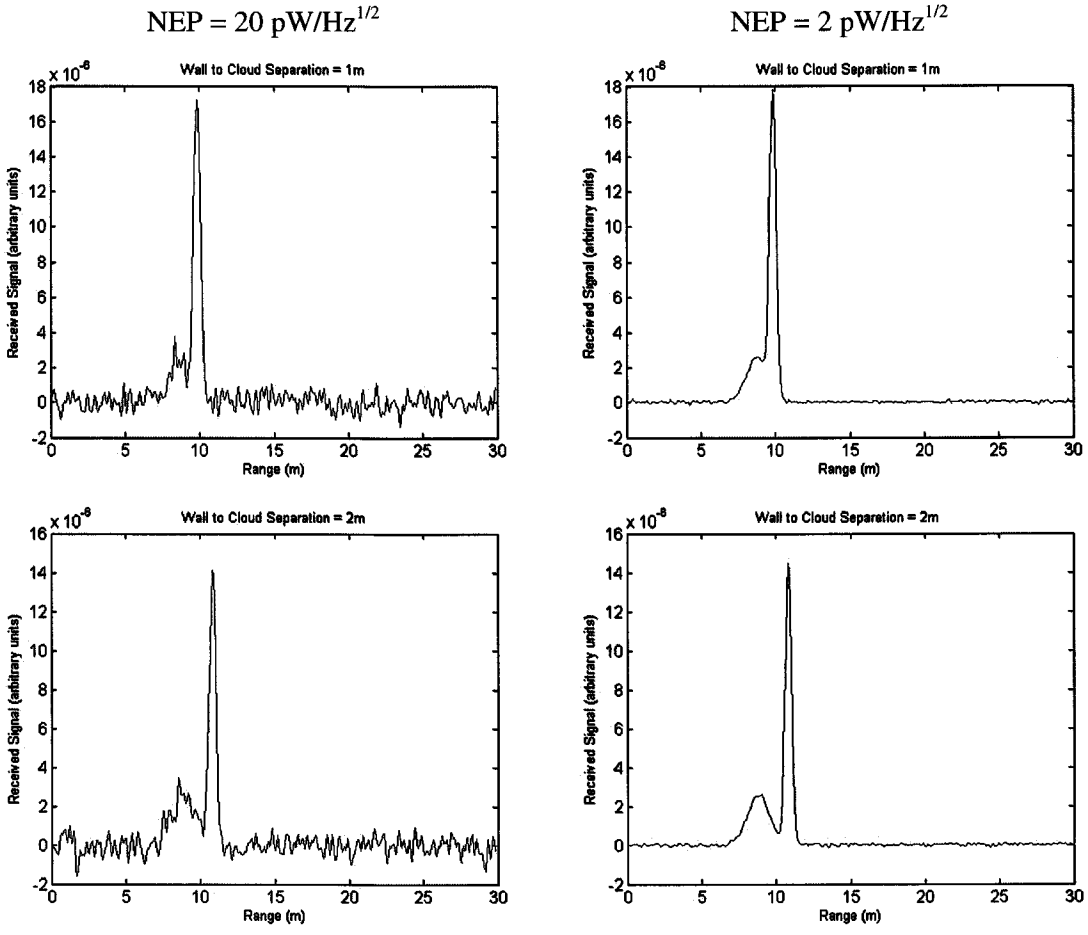

Figure 12. Modeling results for aerosol plume detection.

[2] R. J. Doviak and D. S. Zrnic, Doppler Radar and Weather Observations, Academic Press, New York, 1993

11. Conclusions and Recommendations

We have conducted an experimental study of a laboratory aerosol backscatter lidar instrument, the results of which can serve as benchmarks for the design of a practical device. Measurements of the detector quantum efficiency and gain, as well as the receiver FOV and throughput, were used to quantify the backscatter results from controlled aerosol releases. In parallel, we have developed a model for performing trade studies. For future work, we recommend incorporating a multiple-beam and scanning approaches into the model as a method to differentiate the plume from glancing solid-surface reflections.

Distribution

1 MS9104 W. R. Bolton, 8227
1 MS9054 T. A. Michalske, 8300
1 MS9054 D. R. Hardesty, 8360
1 MS9056 W. L. Hsu, 8368
1 MS9056 T. A. Reichardt, 8368
1 MS9056 R. P. Bambha, 8368
1 MS9104 K. L. Schroder, 8227

3 MS9018 Central Technical File, 8945-1
1 MS0899 Technical Library, 9616
1 MS9021 Classification Office, 8511 for Technical Library, MS 0899, 9616 DOE/OSTI via URL
1 MS0188 D. Chavez, LDRD Office, 1030